INSTITUTE OF PHYSICS PUBLISHING INVERSE PROBLEMS

Inverse Problems **21** (2005) 857–877 doi:10.1088/0266-5611/21/3/005

Pulsed thermography in the evaluation of an aircraft composite using 3D thermal quadrupoles and mathematical perturbations

A Bendada[1], **F Erchiqui**[2] **and M Lamontagne**[1]

[1] National Research Council of Canada, 75 De Mortagne Blvd., Boucherville, QC J4B 6Y4, Canada
[2] University of Quebec in Abitibi-Temiscamingue, 445 Université Blvd., Rouyn-Noranda, QC J9X 5E4, Canada

Received 2 August 2004, in final form 3 August 2004
Published 21 March 2005
Online at stacks.iop.org/IP/21/857

Abstract

This paper is devoted to the characterization of a subsurface flaw within an anisotropic medium during a nondestructive evaluation test using stimulated infrared thermography. A typical illustration is a delamination within a stratified composite material. The originality of the current study consists of providing simple analytical solutions to evaluate the depth and the volume of the flaw in a three-dimensional heat transfer configuration. The volume of the flaw is defined as the product of its lateral extent by its thickness. If the thermal contact resistance of the flaw is known, its lateral extent can be derived from the volume expression. The method proposed here consists of applying first a Laplace transform on the time variable t, then a Fourier transform on the space variables, x and y. The numerical or semi-analytical true solution of integral equations generated by this problem may be very time-consuming, especially in a three-dimensional configuration. We therefore suggest a modelling reduction using the analytical perturbation method written only at its first order. It is however assumed that flaw thermal resistance is small compared to the whole thermal resistance of the material under investigation. The perturbation formalism leads to the construction of approximate analytical solutions that are very convenient for quantitative inversion. The validity of this method has been analysed through a real nondestructive test performed on a calibrated carbon-epoxy laminate of known characteristics.

(Some figures in this article are in colour only in the electronic version)

1. Introduction

In recent years, the study of laminated composites has been of great interest in applied science and engineering owing to their widespread use in various industrial fields (aerospace, nuclear, microelectronics, etc). Complex manufacturing processes of such materials increase the risk

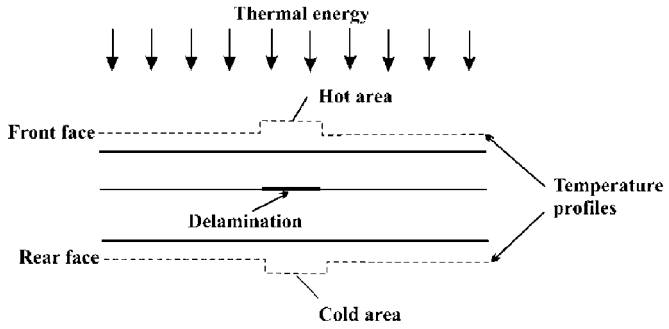

Figure 1. Stimulated infrared thermography principle.

of flaw appearance whose consequences may be crucial. In most cases, the control of their quality is needed to be nondestructive in order to allow inspection during different times of the part's life. In this quality investigation, methods based on heat transfer may be very effective [1–14]. Stimulated infrared thermography is one of the alternatives that may be applied for that purpose. In this technique, the composite sample is irradiated by a uniform heat pulse on one face while the transient temperature either on the same face or on the opposite one is recorded using an infrared camera (figure 1). The temperature difference between the pixel of interest on the infrared frame and a reference area considered sound on the same frame represents a signature of the subsurface flaw. It is this signal, usually called the contrast thermogram, which is commonly used to detect and quantify the flaw. The flaw characterization is carried out using the contrast as an input to an inverse algorithm. To accurately identify the discontinuity features, three stages have to be considered. The first step is to develop a forward model which consists of describing the contrast field evolution in a mathematical formalism as accurately simply and rapidly as possible. The following step is to conceive a measurement procedure which outputs the most correct and least noisy signal. The last step is to develop an inverse problem that estimates the unknown parameters in such a way that the deviation between the experimental data and the forward problem is minimum [15–17]. In this work, we propose a new modelling approach based on the use of the 3D thermal quadrupole formalism [18]. Three-dimensional thermal quadrupoles are obtained by applying to the real temperature field a Laplace transform in the time domain; then a double Fourier transform in the space domain is applied to the previous Laplace temperature field. After the last three integral transforms, the temperature field is treated in the Laplace–Fourier–Fourier image domain. Air delaminations in laminated composites are thermally characterized by a thermal contact resistance. When this resistance is small compared with the material whole resistance, a perturbation method [19–22] can be combined with the thermal quadrupole formalism to yield simple analytical solutions of the nondestructive experiment. The perturbation procedure is based on an asymptotic expansion of the physical field (temperature or heat flux) versus a small parameter intervening in the model. The analytical solutions obtained via this method are very convenient for the development of new inversion procedures which characterize the subsurface flaw within a three-dimensional heat transfer configuration.

2. Theory

2.1. Forward problem

2.1.1. Formulation of the forward problem using 3D thermal quadrupoles. The case of a rectangular ($L \times \ell$) flat sample of thickness e that contains a resistive flaw of finite width

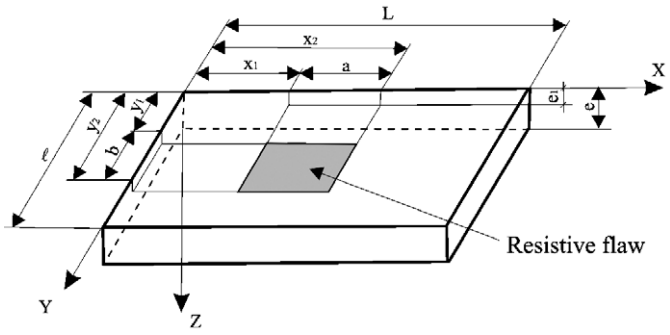

Figure 2. Geometric sketch of a limited extent flaw within an anisotropic material: e_1 = flaw depth; e = total thickness; a = flaw length; b = flaw width; L = specimen length; ℓ = specimen width; z = direction of the heating radiation; x_1, x_2, y_1, y_2 = flaw border coordinates.

a and finite length b, with a uniform contact resistance R_c on its whole area, is typical of a delamination in a composite stratified material (figure 2). In a typical pulsed infrared thermography test, one can assume that: (1) the thermal excitation of the sample is a Dirac distribution characterized by a uniform absorbed energy Q (at time $t = 0$); (2) the front face of the sample is adiabatic; (3) the sample temperature is zero before excitation. Since only the face temperatures are of interest, the quadrupole technique is the easiest formalism to implement to describe the heat transfer. Thermal quadrupoles are obtained after performing a Laplace integral transform on the time variable t, and a double Fourier integral transform on the space variables x and y [23, 24]. Heat transfer modelling of multi-layer materials is then reduced to a simple multiplication of matrices in the transformed Laplace–Fourier–Fourier domain.

If the initial temperature is uniform and if the heat losses are neglected, the Laplace transform $\tau(x, y, z, p)$ (where p is the Laplace variable) of the temperature $T(x, y, z, t)$ in the sample is the solution of the following set of equations:

$$\frac{\partial^2\tau}{\partial z^2} + \frac{\lambda_x}{\lambda_z}\frac{\partial^2\tau}{\partial x^2} + \frac{\lambda_y}{\lambda_z}\frac{\partial^2\tau}{\partial y^2} - \frac{p}{a_z}\tau = 0 \tag{1a}$$

$$x = 0, L \quad \rightarrow \quad \frac{\partial\tau}{\partial x} = 0 \tag{1b}$$

$$y = 0, l \quad \rightarrow \quad \frac{\partial\tau}{\partial y} = 0 \tag{1c}$$

$$z = 0 \quad \rightarrow \quad -\lambda_z\frac{\partial\tau}{\partial z} = Q \tag{1d}$$

$$z = e_1 \quad \rightarrow \quad \frac{\partial\tau^{\text{sup}}}{\partial z} = \frac{\partial\tau^{\text{inf}}}{\partial z} \tag{1e}$$

$$\tau^{\text{sup}} - \tau^{\text{inf}} = R_c s(x, y)\left[-\lambda_z\frac{\partial\tau}{\partial z}\right] \tag{1f}$$

$s(x, y) = 1$ if $(x, y) \in \{[x_1, x_2] \times [y_1, y_2]\}$ and $s(x, y) = 0$ elsewhere.

Superscripts 'sup' and 'inf' relate to the upper and lower face of the flaw

$$z = e \quad \rightarrow \quad \frac{\partial\tau}{\partial z} = 0. \tag{1g}$$

The analysis can simultaneously be performed for both isotropic and anisotropic (providing that the sample faces are parallel to the main directions of anisotropy) materials by using the following dimensionless governing parameters:

$$\tau^* = \tau(Qe/\lambda_z) \qquad a^* = \frac{a}{e}(\lambda_z/\lambda_x)^{1/2}$$

$$\psi^* = \psi/Q \qquad b^* = \frac{b}{e}(\lambda_z/\lambda_y)^{1/2}$$

$$x^* = \frac{x}{e}(\lambda_z/\lambda_x)^{1/2} \qquad p^* = e^2 p/a_z$$

$$y^* = \frac{y}{e}(\lambda_z/\lambda_y)^{1/2} \qquad R_c^* = R_c/(e/\lambda_z)$$

$$z^* = z/e \qquad e_1^* = e_1/e$$

where ψ is the Laplace transform of the z component of the heat flux density φ ($= -\lambda_z \partial T/\partial z$). In the remaining text of this paper, the asterisk superscript in the above parameters will be omitted for clarity reasons. The partial differential equation (1*a*) then becomes

$$\frac{\partial^2 \tau}{\partial z^2} + \frac{\partial^2 \tau}{\partial x^2} + \frac{\partial^2 \tau}{\partial y^2} - p\tau = 0. \tag{2}$$

The next step is to apply a Fourier transform to the function $\tau(x, y, z, p)$. The lateral boundary conditions determine the type of transform to carry out [25]; in our case it is a cosine shape

$$q(\alpha, \beta, z, p) = \int_0^L \int_0^\ell \tau(x, y, z, p) \cos(\alpha x) \cos(\beta y)\, \mathrm{d}x\, \mathrm{d}y. \tag{3}$$

As for the boundary conditions on the opposite faces $x = L$ and $y = \ell$, they determine the discrete values allowed for the space frequencies: $\alpha_j = j\pi/L$, $\beta_k = k\pi/\ell$, j and k are non-negative integers.

Using equation (3) and the lateral boundary conditions, equation (2) yields

$$\frac{\mathrm{d}^2\theta}{\mathrm{d}z^2} - (p + \alpha^2 + \beta^2)\theta = 0. \tag{4}$$

The solution of equation (4) has the following form:

$$\theta = F \cosh(uz) + G \sinh(uz) \tag{5}$$

where $u = \sqrt{p + \alpha^2 + \beta^2}$, and F and G are two constants that can be determined using the boundary and interface conditions in z. If θ is known, back inversion into the Laplace domain is given by

$$\tau(x, y, z, p) = \frac{1}{L\ell}\left[\theta_{00} + 2\sum_{j=1}^{\infty} \theta_{j0} \cos(\alpha_j x) + 2\sum_{k=1}^{\infty} \theta_{0k} \cos(\beta_k y) + 4\sum_{j=1}^{\infty}\sum_{k=1}^{\infty} \theta_{jk} \cos(\alpha_j x) \cos(\beta_k y)\right] \tag{6}$$

where $\theta_{jk} = \theta(\alpha_j, \beta_k, z, p)$.

If Φ is the Fourier transform of the Laplace heat flux density Ψ, which is unity at $z = 0$ and zero at $z = 1$ (equations (1*d*) and (1*g*)) we obtain

$$z = 0 \quad \rightarrow \quad \Phi(\alpha, \beta, 0, p) = \frac{\sin(\alpha L)}{\alpha} \frac{\sin(\beta l)}{\beta} \tag{7}$$

$$z = 1 \quad \rightarrow \quad \Phi(\alpha, \beta, 1, p) = 0. \tag{8}$$

If the arguments other than z are omitted in the Laplace–Fourier transforms θ and Φ, this equation leads to a linear relationship between the two quantities on the front ($z = 0$) and rear ($z = 1$) faces

$$\theta(0) = A\theta(1) + B\Phi(1) \tag{9a}$$

$$\Phi(0) = C\theta(1) + D\Phi(1). \tag{9b}$$

Boundary conditions (1d) to (1g) can be rewritten under the following matrix forms, commonly called quadrupoles [18]:

$$\begin{bmatrix} \theta(0) \\ \frac{\sin(\alpha L)}{\alpha}\ \frac{\sin(\beta l)}{\beta} \end{bmatrix} = \begin{bmatrix} A_1 & B_1 \\ C_1 & D_1 \end{bmatrix} \begin{bmatrix} \theta^{\sup} \\ \Phi(e_1) \end{bmatrix} \tag{10a}$$

$$\begin{bmatrix} \theta^{\sup} \\ \Phi(e_1) \end{bmatrix} = \begin{bmatrix} \theta^{\inf} + R_c I \\ \Phi(e_1) \end{bmatrix} \tag{10b}$$

$$\begin{bmatrix} \theta^{\inf} \\ \Phi(e_1) \end{bmatrix} = \begin{bmatrix} A_2 & B_2 \\ C_2 & D_2 \end{bmatrix} \begin{bmatrix} \theta(1) \\ 0 \end{bmatrix} \tag{10c}$$

where

$$I = \int_{x_1}^{x_2} \int_{y_1}^{y_2} \psi(x, y, e_1, p) \cos(\alpha x) \cos(\beta y)\, \mathrm{d}x\, \mathrm{d}y \tag{10d}$$

$$A_i = D_i = \cosh(ue_i), \qquad B_i = \frac{1}{u}\sinh(ue_i), \qquad C_i = u\sinh(ue_i) \qquad \text{for} \quad i = 1, 2$$

where e_1 and e_2 are the thicknesses of the two layers of the sample.

A true solution of (10) can be found if the heat flux at the interface $\Phi(e_1)$ is known. Fourier components of the latter are obtained by solving a linear set of equations. This one is built up by substituting the Laplace heat flux $\Psi(e_1)$ into the integral I of equation (10d) by the inverse Fourier series allowing its calculation from a given $\Phi(e_1)$. But in many cases, this method is very time-consuming, particularly in three-dimensional analyses [25]. In the following section, we present a simpler and faster method to solve the same problem; it is the perturbation method [19–22].

2.1.2. Resolution of the forward problem using mathematical perturbations. The perturbation method consists of writing asymptotic series expansions of the variables θ and Φ with respect to a small parameter in the model. These series expansions are then injected into set 10, and term-by-term identification of the coefficients of the successive powers of the small parameter leads to a coupled series of linear sets. These allow the calculation of the different components θ_i and Φ_i. The mathematical formalism presented below is valid only for small values of the thermal contact resistance R_c. The asymptotic series expansions with respect to the small parameter R_c that will be noted ε from now on are

$$\theta(\alpha, \beta, z, p) = \sum_{i=0}^{\infty} \theta_i(\alpha, \beta, z, p)\varepsilon^i \tag{11a}$$

$$\Phi(\alpha, \beta, z, p) = \sum_{i=0}^{\infty} \Phi_i(\alpha, \beta, z, p)\varepsilon^i. \tag{11b}$$

Term-by-term identification of the coefficients of ε^n leads to the following quadrupole equations:

ε^0-order identification. For zero order, set 9 results in

$$\begin{bmatrix} \theta_0(0) \\ \frac{\sin(\alpha L)}{\alpha}\ \frac{\sin(\beta l)}{\beta} \end{bmatrix} = \begin{bmatrix} A_1 & B_1 \\ C_1 & D_1 \end{bmatrix} \begin{bmatrix} A_2 & B_2 \\ C_2 & D_2 \end{bmatrix} \begin{bmatrix} \theta_0(1) \\ 0 \end{bmatrix}. \tag{12}$$

This zero-order term obviously represents the one-dimensional heat transfer within a sane plate. As we will further see, the perturbation analysis requires the zero-order Laplace flux to be known within the sane plate at the flaw depth. It is merely extracted from equation (12)

$$\psi_0(e_1) = \sinh(\sqrt{p}e_2)/\sinh(\sqrt{p}). \tag{13}$$

ε^1-order identification. For ε^1 order, set 10 turns out to be

$$\begin{bmatrix} \theta_1(0) \\ 0 \end{bmatrix} = \begin{bmatrix} A_1 & B_1 \\ C_1 & D_1 \end{bmatrix} \begin{bmatrix} \theta_1^{\sup} \\ \Phi_1(e_1) \end{bmatrix} \tag{14a}$$

$$\begin{bmatrix} \theta_1^{\sup} \\ \Phi_1(e_1) \end{bmatrix} = \begin{bmatrix} \theta_1^{\inf} + I_0 \\ \Phi_1(e_1) \end{bmatrix} \tag{14b}$$

$$\begin{bmatrix} \theta_1^{\inf} \\ \Phi_1(e_1) \end{bmatrix} = \begin{bmatrix} A_2 & B_2 \\ C_2 & D_2 \end{bmatrix} \begin{bmatrix} \theta_1(1) \\ 0 \end{bmatrix} \tag{14c}$$

I_0 has the same definition as I in equation (10*d*), just replacing Ψ by Ψ_0. The substitution of Ψ_0 defined by equation (13) into this definition allows the calculation of integral I_0 and therefore the solution of set 14. The first-order temperature on the rear face is given by

$$\theta_1(1) = -\frac{4}{\alpha\beta} K \frac{\sinh(ue_1)\sinh(\sqrt{p}e_2)}{\sinh(\sqrt{p})\sinh(u)} \tag{15}$$

where

$$K = \sin\left(\alpha\frac{x_2 - x_1}{2}\right)\cos\left(\alpha\frac{x_1 + x_2}{2}\right)\sin\left(\beta\frac{y_2 - y_1}{2}\right)\cos\left(\beta\frac{y_1 + y_2}{2}\right).$$

The front face temperature can be calculated in the same way

$$\theta_1(0) = \frac{4}{\alpha\beta} K \frac{\sinh(ue_2)\sinh(\sqrt{p}e_2)}{\sinh(\sqrt{p})\sinh(u)}. \tag{16}$$

Products of equations (15) and (16) by ε represent the Laplace–Fourier transforms $\Delta\theta = \varepsilon\theta_1$ of the contrast $\Delta T(x, y, z_s, t)$ on the rear and front face, respectively. Return to the original (x, y, z_s, t) domain can be achieved numerically by using fast-Fourier-transform (FFT) and Stehfest [26] algorithms. The concept of thermal contrast is very important in nondestructive evaluation by stimulated thermography, which represents the aim of the current work. An interesting property of the contrast function ΔT (positive for the front face measurement and negative for the rear face measurement) lies in the fact that it cancels out in the absence of contact resistance R_c; it is therefore a signature of the hidden flaw. Let us remind the reader here that the modelling described previously is based on the assumption of an adiabatic heat transfer. In reality, nondestructive experiments are always affected by heat losses. Their effect on thermal contrasts obtained in nondestructive testing via infrared thermography has already been reported in the scientific literature [27]. The authors thoroughly compared the adiabatic case with the case where heat losses are present and characterized with a heat transfer coefficient $h = 20\ \mathrm{W\ m^{-2}\ K^{-1}}$. Simulations were performed for a wide enough flaw that was

characterized with a normalized contact resistance $R_c = 0.08$. The normalized depth e_1 of the flaw was considered as a variable parameter and changed from 0 to 1. The authors showed that there was practically no effect on the front face contrast whereas only a slight decrease, around 6%, could be observed on the extreme value $\Delta T_{\max}$ of the rear face contrast. The common heat transfer coefficients at room temperature are generally around 10 W m $^{-2}$ K^{-1}, which means that the contrast deviation observed above is overestimated. This very small effect of heat losses is a consequence of the nature of the thermal contrast itself: even if each surface temperature T and T_0 might be strongly affected by heat losses, their difference, $\Delta T = T - T_0$, leads in general to a compensation for this effect.

Furthermore, the analytical formulae (15) and (16) are very simple even in this three-dimensional transient heat transfer situation. Numerical simulations have been carried out in a previous work [28] to assess the effectiveness of the above model. The simulations have shown that the perturbed contrast profiles are in excellent agreement with the true ones for small thermal resistance values, up to $\varepsilon = 0.3$. However, for higher resistances ($\varepsilon > 0.3$) the approximation is no longer appropriate, confirming the restriction of the above model to weak flaws. It is worth noting here that $\Delta\theta$ is linear in ε, which means that for small ε' the contrasts produced by two discontinuities, for example of resistances ε_1 and ε_2 located at distinct depths with different lateral extents (i.e. a multi-delamination in an impacted composite [25, 29]), simply add up. Nevertheless, this is not the case for the temperature. Indeed, this can be inferred from the Laplace temperature for two superimposed flaws according to

$$\tau(x, y, 1, p) = \frac{\cosh(\sqrt{p})}{\sqrt{p}\sinh(\sqrt{p})}\{1 + \varepsilon_1 f_1 + \varepsilon_2 f_2\} + O(\varepsilon) \tag{17}$$

where $f_m(x, y, 1, p)$ is the inverse Fourier transform of $\theta_1(1)$ multiplied by $\sqrt{p}\sinh(\sqrt{p})$. The f_m function is written using the location parameters of the flaw number m ($m = 1, 2$). We note here that equation (17) can also be written by substituting, in its right-hand side, the term between braces by its [0, 1] Padé's approximant, namely $\{1 - \varepsilon_1 f_1 - \varepsilon_2 f_2\}^{-1}$. The $[P, Q]$ Padé's approximant of a series $S(\varepsilon) = \sum_{n=0}^{\infty} c_n \varepsilon^n$ is the rational fraction in ε, with a numerator of degree P and a denominator of degree Q, such as its expansion into a Taylor's series coincides with the series $S(\varepsilon)$ [30]. The use of Padé's approximant has the advantage of 'sticking' the solution to the true model for larger ε_m's while being equivalent to equation (15) for small values of these parameters. Numerical simulations performed in a previous work [28] have shown that the latter approach widened the validity of the first-order perturbation method to larger ε values, up to $\varepsilon = 0.5$.

2.2. Explicit evaluation procedures

In the following, we describe the inversion procedures that allow the evaluation of the depth and the volume of the subsurface flaw. These parameters are directly derived from the perturbation 3D modelling described in the previous subsection. Recall that the perturbation modelling is valid only under the assumption of small thermal contact resistances ε.

2.2.1. Evaluation of the volume of the flaw. In this subsection, we show how the volume of the flaw can be derived from the space averaging of the Laplace contrast profile $\Delta\tau(x, y, z_s, p)$, if the depth of the flaw e_1 is already known. The volume V of the flaw is defined as the product of its lateral extent $a \times b$ and its thickness e_f, $v = a \times b \times e_f$. Furthermore, the thermal contact resistance per surface unit is defined as the ratio of the flaw thickness e_f and its thermal conductivity λ_f, $\varepsilon = e_f/\lambda_f$,. The volume of the flaw can then be written under the following form: $v = a \times b \times \varepsilon \times \lambda_f$. For a delamination within a composite material, λ_f is

simply the thermal conductivity of the air, which is a known parameter, trapped between the material layers. Evaluation of the volume v of the flaw is therefore equivalent to the estimation of the product of its lateral extent by its thermal resistance, $a \times b \times \varepsilon$. The space average of the Laplace contrast is defined as

$$\Delta\bar{\tau} = \frac{1}{L\ell}\int_0^L\int_0^\ell \Delta\tau(x, y, z_s, p)\,\mathrm{d}x\,\mathrm{d}y \tag{18}$$

$$\text{with} \quad z_s = 0 \text{ (front face)} \quad \text{or} \quad z_s = 1 \text{ (rear face)}$$

where $\Delta\bar{\tau}$ is the difference between the Laplace transform of the temperature on one spot of the face of the sample and its value in the absence of any flaw. With the previous first-order perturbation method, the integral in the right-hand side of equation (18) is equal to $\varepsilon\theta_1(0, 0, z_s, p)$. Application of equations (15) and (16) allow the calculation of $\Delta\bar{\tau}$ for each face:

$$\Delta\bar{\tau}(1, p) = -\frac{\varepsilon ab}{L\ell}\frac{\sinh(\sqrt{p}e_1)\sinh[\sqrt{p}(1-e_1)]}{\sinh^2(\sqrt{p})} \tag{19}$$

$$\Delta\bar{\tau}(0, p) = \frac{\varepsilon ab}{L\ell}\frac{\sinh^2[\sqrt{p}(1-e_1)]}{\sinh^2(\sqrt{p})}. \tag{20}$$

These show that the average Laplace contrast (and therefore the instantaneous averaged contrast $\Delta\bar{\tau}$) is proportional to the product of the area $a \times b$ and the thermal resistance ε of the flaw. In other words, the average Laplace contrast is proportional to the flaw volume. Application of equation (19) or (20) may lead to the determination of the flaw volume v if its depth e_1 is known. It is worth noting here that for a better approximation in the case of larger thermal resistances, equation (19) can be written into the following form:

$$\Delta\bar{\tau}(1, p) = \frac{1}{\sqrt{p}\sinh(\sqrt{p})}\left[\frac{1}{1+\varepsilon F(p)} - 1\right] \tag{21}$$

where

$$F(p) = \frac{ab}{L\ell}\sqrt{p}\frac{\sinh(\sqrt{p}e_1)\sinh(\sqrt{p}(1-e_1))}{\sinh(\sqrt{p})}. \tag{22}$$

A similar form can be found for the front face average contrast in equation (20)

$$\Delta\bar{\tau}(0, p) = \frac{\coth(\sqrt{p})}{\sqrt{p}}\left[\frac{1}{1-\varepsilon G(p)} - 1\right] \tag{23}$$

where

$$G(p) = \frac{ab}{L\ell}\frac{\sqrt{p}}{\coth(\sqrt{p})}\frac{\sinh^2(\sqrt{p}(1-e_1))}{\sinh(\sqrt{p})}. \tag{24}$$

2.2.2. Extension to the evaluation of the lateral area of the flaw when heat transfer upon the centre of the flaw is one dimensional. Let us note here that the flaw volume is an important information, but usually industrial requirements focus on thresholds on lateral extent $a \times b$ and thermal contact resistance ε. From equations (19) and (20), it can clearly be seen that the thermal contact resistance and the lateral extent of the flaw are correlated and therefore $a \times b$ cannot be derived from these equations without knowing the value of ε, and vice versa. Fortunately, in some cases where heat transfer across the central area of the flaw can be considered one dimensional, it is possible to get rid of this correlation issue and to quantify

the thermal resistance ε independently from the lateral extent $a \times b$. According to a previous work [31] where modelling was performed with numerical codes, the assumption of one-heat transfer is true only for wide enough flaws (i.e. lateral extent $a \times b > 2 \times 2$). The expression of the one-dimensional Laplace contrast $\Delta\tau(x_c, y_c, z_s, p)$ at the centre (x_c, y_c) of the flaw can be derived from equations (19) and (20). The one-dimensional Laplace contrast $\Delta\tau(x_c, y_c, z_s, p)$ at the centre (x_c, y_c) of the flaw is equal to the average Laplace contrast when the lateral extents of the flaw and the sample are the same (i.e. $a \times b = L \times \ell$).

For the rear face approach for example, the one-dimensional Laplace contrast at the centre of a flaw of large enough lateral extent $a \times b$ is given by

$$\Delta\tau(x_c, y_c, 1, p) = -\varepsilon \frac{\sinh(\sqrt{p}e_1)\sinh[\sqrt{p}(1-e_1)]}{\sinh^2(\sqrt{p})}. \tag{25}$$

Equation (25) depends on two unknowns: the thermal resistance ε, and the depth e_1. If it is written for two values p_1 and p_2 $(= 4p_1)$ of the Laplace variable, the parameter e_1 can then be eliminated from the two corresponding equations by using the duplication properties of the hyperbolic functions. If n_1 and n_2 are the experimental Laplace contrasts on the rear face at the centre of the flaw, the thermal resistance of the flaw is given by the following equation:

$$\varepsilon = \frac{n_1^2 \sinh(\sqrt{p_1})\tanh(\sqrt{p_1})}{n_2\cosh(\sqrt{p_1}) - n_1} \tag{26}$$

where

$$n_i = \Delta\tau(x_c, y_c, 1, p_i), \qquad i = 1, 2 \qquad \text{and} \qquad p_2 = 4p_1.$$

2.2.3. Evaluation of the depth of the flaw. It can be observed from equation (19) that a flaw located either at a depth e_1 or $(1 - e_1)$ gives rise to the same thermal contrast on the rear face of the sample. This means that depth inversion from the rear signal does not have a single solution; only resistance identification can be conceivable. This is not the case for the front face thermal contrast; equation (20) shows that for each depth the thermal contrast is different. Owing to the latter remarks, it is clear that the best way to recover a unique solution for the unknown flaw depth is to use the front face contrast. A procedure similar to that adopted in the previous section for the estimation of the thermal resistance is carried out here for the evaluation of the flaw depth from the 3D heat transfer model. Equation (20) written for two values p_1 and p_2 $(= 4p_1)$ yields the analytical elimination of the unknown parameters ε and $a \times b$. If $\bar{m}_1$ and $\bar{m}_2$ are the experimental average Laplace contrasts on the front face, the depth e_1 of the flaw is the solution of the following equation:

$$\cosh(\sqrt{p_1}(1-e_1)) = \left(\frac{\bar{m}_2}{\bar{m}_1}\right)^{1/2} \cosh(\sqrt{p_1}) \tag{27}$$

where

$$\bar{m}_i = \Delta\bar{\tau}(x, y, 0, p_i) \qquad \text{and} \qquad i = 1, 2.$$

This equation leads to the following estimation of the flaw depth:

$$e_1 = 1 - \frac{1}{\sqrt{p_1}} \ln\left[\left(\frac{\bar{m}_2}{\bar{m}_1}\right)^{1/2} \cosh(\sqrt{p_1}) + \left(\frac{\bar{m}_2}{\bar{m}_1}\cosh^2(\sqrt{p_1}) - 1\right)^{1/2}\right]. \tag{28}$$

It worth noting for reference that the determinations of the depth and the resistance of the flaw cannot be done simultaneously from the front face signal. That is because it has been shown that the two parameters are correlated in a front face experiment, which makes their simultaneous estimation hazardous from front face contrasts [27, 32]. And since the flaw depth can be evaluated only from front face experiments, the optimal inversion procedure

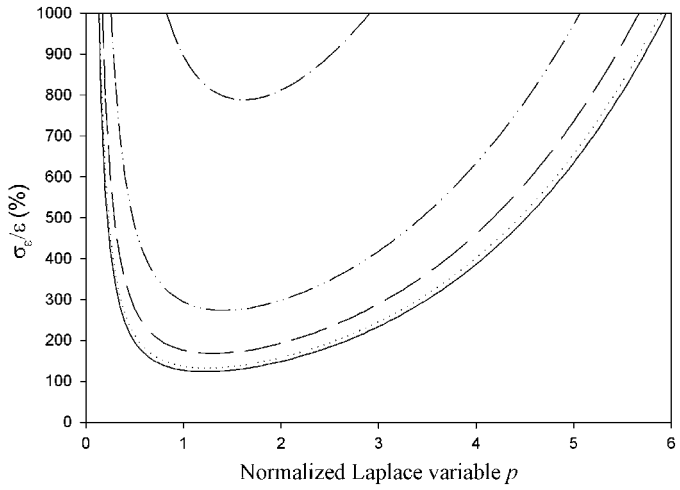

Figure 3. Theoretical estimation uncertainty on the thermal contact resistance of the flaw ε ((——): $e_1 = 0.5$; (· · · · · ·): $e_1 = 0.4$; (- - - -): $e_1 = 0.3$; (— · · —) line: $e_1 = 0.2$; (— · —): $e_1 = 0.1$).

should then be to estimate the resistance by using a rear face experiment and the depth starting from a front face experiment.

2.3. Statistical analysis of the accuracy of the inversion procedures

Any inversion algorithm produces estimated parameters. A measurement of the quality of the inversion requires a compulsory quantification of the estimation error that has been made. In this work, this error can be divided into two parts: the error caused by measurement noise, and the error caused by performing the quadratures, in time to calculate the Laplace transform and in space to calculate the average Laplace contrast, on a limited number of points ($\sum$ instead of $\int$). In the following, this second error will be neglected since the numbers of points, in time and space, used to perform the quadratures are considered large enough. Using a stochastic analysis with the assumptions that the noise on the thermal contrast ΔT is additive, uncorrelated and of constant standard deviation σ, we can quantify the inversion errors caused by measurement noise.

2.3.1. Estimation error during thermal resistance inversion. The effect of measurement noise on the precision of the thermal resistance estimated via a rear face experiment is calculated via a statistic procedure in appendix C. It is represented by the variance of the thermal resistance described by equation (C.7). In figure 3, the relative standard deviation, $\sigma_\varepsilon/\varepsilon$, of the thermal resistance is reported as a function of the Laplace variable p ($=p_1$) for different values of the flaw depth. Since the rear face contrast is the same for a flaw located at a depth e_1 or $1 - e_1$, only curves that correspond to depths in the range 0.1–0.5 are presented. With regard to the rest of parameters in equation (29), we used a standard deviation of the normalized ΔT contrast $\sigma = 0.1$ calculated for a maximum temperature rise of 4 °C after the heating and a measurement noise of the infrared camera of 0.2 °C. We also used a normalized time step $\Delta t = 4 \times 10^{-3}$ that corresponds to a scan rate of 40 ms, a carbon-epoxy plate that is 2 mm thick, and a thermal resistance $\varepsilon = 0.073$. We can note from the figure that: (1) the optimum p-value that should be used for thermal resistance inversion independently from the flaw depth must be within the range 1–2, (2) the closer the flaw from the sample faces the worse the

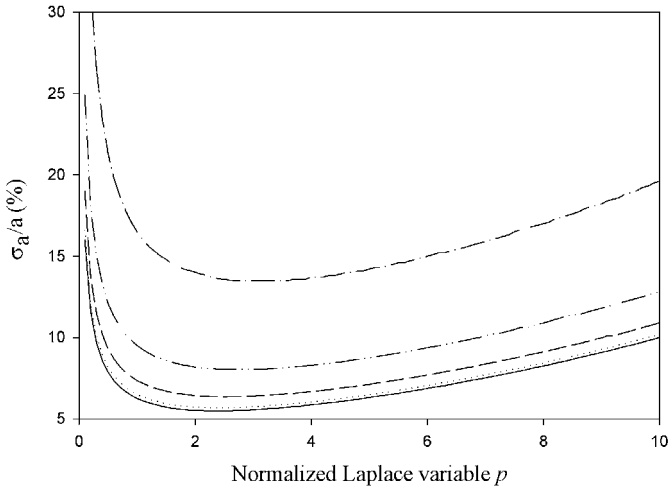

Figure 4. Theoretical estimation uncertainty on the flaw depth e_1 ((——): $e_1 = 0.1$; (· · · · · ·): $e_1 = 0.3$; (- - - -): $e_1 = 0.4$; (— · · —): $e_1 = 0.6$; (— · —): $e_1 = 0.7$).

estimation of the thermal resistance; for optimum p-values the error changes from ∼125% for $e_1 = 0.5$ up to ∼800% for $e_1 = 0.1$ or 0.9, (3) the ill-posedness of the inverse problem can clearly be observed by the strong nonlinear variation of the estimation error versus flaw depth, as well as by the its importance, >125%, even for flaws located at mid-depth, (4) the inversion procedure is not very robust since the estimation errors are quite high.

2.3.2. Estimation error during depth inversion. The effect of measurement noise on the precision of the flaw depth estimated via a front face experiment is calculated via a statistic procedure in appendix D. It is represented by the variance of the flaw depth described by equation (D.7). In figure 4, we reported the relative standard deviation, σ_{e_1}/e_1, of the normalized depth versus the Laplace variable p ($= p_1$) for different values of the flaw depth. The size of the sample was assumed to be 60 mm × 60 mm, the size of the flaw 10 mm × 10 mm, and the numbers M and N are 190 and 105, respectively. The latter parameters were chosen to be the same as those used in the experimental validation described below. The rest of the parameters were the same as the previous simulation described in subsection 2.3.1. One can observe that: (1) the choice of the optimum p-value depends on the depth e_1, but it is always in the range 1–2 for deep flaws; for flaws close to the surface ($e_1 = 0.1$, 0.2, 0.3) the error is negligible beyond p-values higher than 1; (2) a bad choice of p leads to a only small error on the precision for flaws located near the heated surface, whereas for deeper flaws, the discrepancies are much higher; (3) the accuracy for a deep flaw and a shallow flaw changes tremendously: as an example for a flaw located at $e_1 = 0.7$, the minimum error (obtained for $p_{\text{opt}} = 1.5$) may exceed 50%, while for a flaw located at $e_1 = 0.3$ the error is only around 5% for the same p-value; (4) the estimation error changes nonlinearly with the Laplace variable p and the flaw depth e_1.

2.3.3. Estimation error during flaw area inversion. The effect of measurement noise on the precision of the flaw area estimated via a rear face experiment is calculated via a statistic procedure in appendix E. It is represented by the variance of the flaw area described by equation (E.3). In figure 5, the relative standard deviation, σ_a/a, of the side a of the flaw

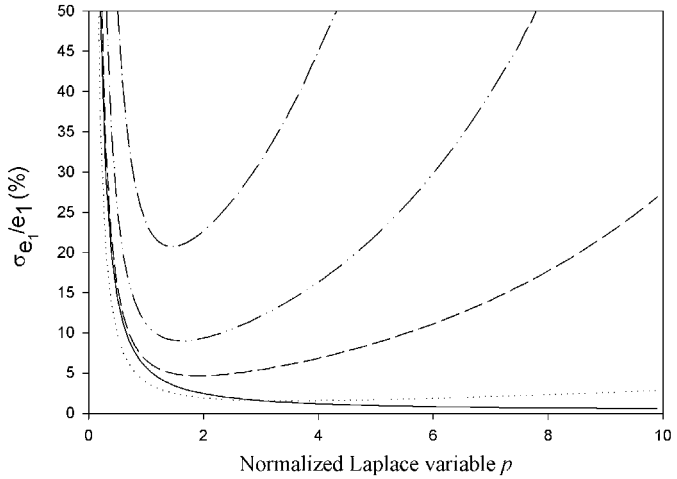

Figure 5. Theoretical estimation uncertainty on the lateral flaw extent a ((——): $e_1 = 0.5$; (· · · · · ·): $e_1 = 0.4$; (- - - -): $e_1 = 0.3$; (— · · —): $e_1 = 0.2$; (— · —): $e_1 = 0.1$).

assumed to be square (i.e. $a = b$ and $S = a^2$), is reported as a function of the Laplace variable p for different values of the flaw depth. For the same reasons as in subsection 2.3.1, only curves that correspond to depths in the range 0.1–0.5 are presented. To perform the theoretical simulation, we used the same parameters as in previous subsection. We note from the figure that: (1) the error changes nonlinearly with the flaw depth, (2) the minimum error is obtained for an optimum p-value around 2 independently from the flaw depth, (3) beyond this optimum value, the error increases very slightly, which extends the range of the optimum p-values that can be used for the inversion without affecting that much its precision, (4) for p-values less than 1, the variation of the error with p is very steep, (5) if the optimum p-value is used for inversion, the estimation error is less than 10% for most flaw depths, for very shallow flaws ($e_1 = 0.1$) the error is around 15%, which is still very acceptable in such NDT investigations.

3. Experimental validation

In order to evaluate the capacity of the perturbation modelling in representing the transient 3D heat transfer in a stimulated thermography experiment, we have compared the results of the analytical perturbation model to those obtained during a real nondestructive testing test.

3.1. Test sample

The test sample is a square slab 60 mm × 60 mm and 2 mm thick, made out of a 14-layer-carbon-epoxy laminate. The two faces of the test sample are not painted with any high emissivity painting. The material is orthotropic and its thermal properties are: $\lambda_z = 0.67$ W m^{-1} K^{-1}, $\lambda_x = \lambda_y = 2.40$ W m^{-1} K^{-1}, $\rho c = 1.62 \times 10^{-6}$ J m^{-3} K^{-1}. The delamination is simulated with a 10 mm × 10 mm square artificial insert made out of two 25 μm thick Teflon films. These inserted films simulate a 3 μm thick delamination located at mid-depth in the sample ($e_1 =$ 0.5). Teflon has a thermal conductivity of 0.23 W m^{-1} K^{-1}. The nominal normalized thermal resistance R_c of the artificial flaw is therefore around 0.073. It is worth noting that the nominal thermal resistance is smaller than 0.3, which allows, according to observations reported in section 2, the application of the perturbation models to the specimen under investigation.

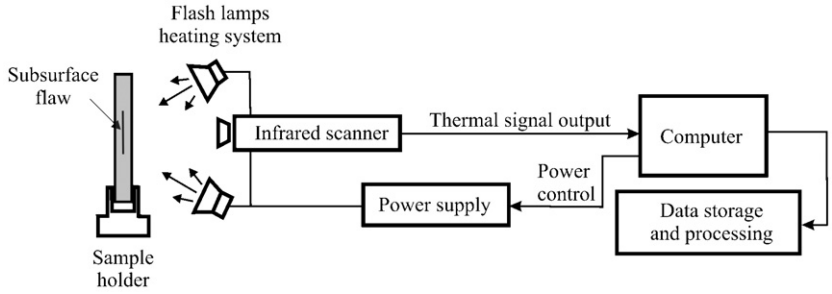

Figure 6. Block diagram of the front face experimental set-up.

3.2. Experimental set-up

A block diagram of the experimental set-up used during front face configurations is shown in figure 6. The rear face configuration is obtained by installing the infrared scanner and the thermal stimulation system on both sides of the sample under investigation. Heat pulse excitation is produced by an assembly of four flash tubes. Each flash tube is located on one side of a 10 cm $\times$ 10 cm square frame. At the rear of each heating flash tube, a parabolic mirror is installed to focus the emitted light onto the sample under investigation. The duration of the photothermal excitation is less than 10 ms for an incident energy Q of 3 to 4 J cm^2.

The temperature field on the faces of the sample after the flash heating is recorded with a Thermovision 782 SW Agema infrared scanner connected to a computer system controller. The infrared scanner is designed to operate in the 3.5–5.6 μm band of the infrared spectrum. However, there is also some response outside this spectral range. The scanner uses an indium antimonide (InSb) detector with Stirling cycle cooling. A 20° lens remotely focused with the system controller keyboard is used with no optical filter. The optical scanning unit synchronization gives a scan rate of 25 images per second and an image resolution of 128 pixels by 64 lines. The temperature range of the scanner can be changed remotely by the selection of different range settings at the system controller. These are achieved in the scanner by both gain control and aperture wheel setting. The range used in the current work is 0–250 °C. The scanner has a sensitivity of 0.08 °C at 30 °C, an accuracy of 1% and a repeatability of 0.5% through the used temperature range. The infrared images are stored in real time on a hard disk for subsequent processing.

3.3. Experimental results and discussion

One rear face and one front face measurement are carried out on the test sample described in section 3.1. The rear face experiment is performed to evaluate the thermal resistance ε and the lateral extent $a \times b$ of the flaw, while the front face experiment is performed to evaluate the flaw depth e_1.

Figure 7 displays a temperature image of the sample recorded 1.4 s after the flash heating in the rear face experiment. The uneven temperature distribution in the image clearly reveals the presence of the subsurface flaw. Averaging the infrared sequence over a period of 2 s yields a better detection of the flaw (figure 8). A quick inspection of this thermographic image allows the choosing of a sane zone where internal flaws do not exist. This reference zone will be used later for the calculation of the thermal contrast which represents the input signal for the estimation procedures developed above.

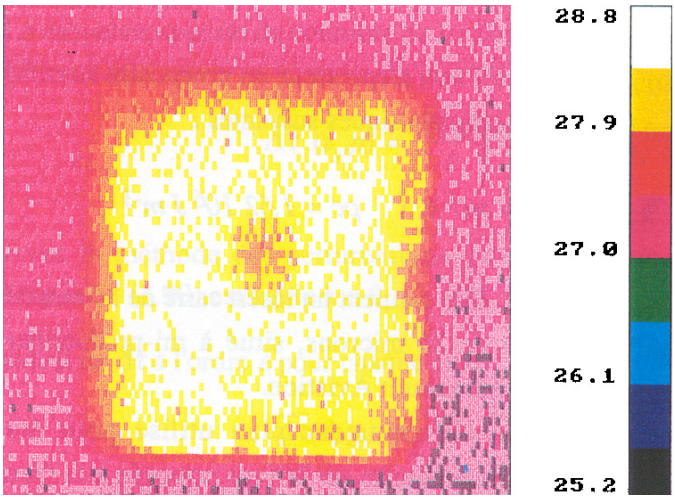

Figure 7. Thermographic image T (°C) at time $t = 1.4$ s after the flash heating in a rear face experiment: time when the contrast reaches a maximum value.

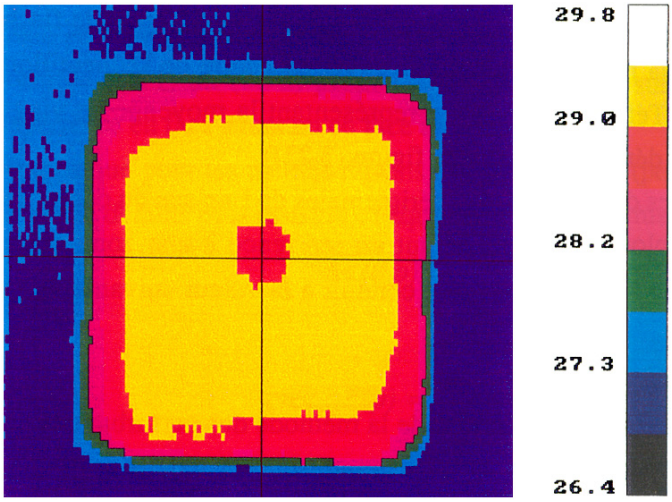

Figure 8. Thermographic image T (°C) obtained by averaging a sequence of instantaneous images over a period of 2 s. The averaging procedure leads to a better signal-over-noise ration, which enhances the detection of the subsurface flaw.

The lateral extent of the artificial flaw is 10 mm $\times$ 10 mm, which yields a nominal normalized extent $a \times b = 2.64 \times 2.64$. According to the observations given in subsection 2.2.1 and the fact that the normalized lateral extent $a \times b > 2 \times 2$, heat transfer across the centre of the flaw is one dimensional. Application of equation (26) with an optimum Laplace variable of 1 in the region of the flaw centre leads to the following value of the normalized thermal resistance: $\varepsilon = 0.185$. This value is about two times and a half higher than the nominal value of the flaw, which is $\varepsilon = 0.073$. The relative deviation between the estimated and theoretical ε values is $\sim$153%. This deviation magnitude may be caused by the effect of measurement noise in the thermograms as was predicted by the statistical analysis described in subsection 2.3.1; the predicted estimation error due to noise for a flaw located at

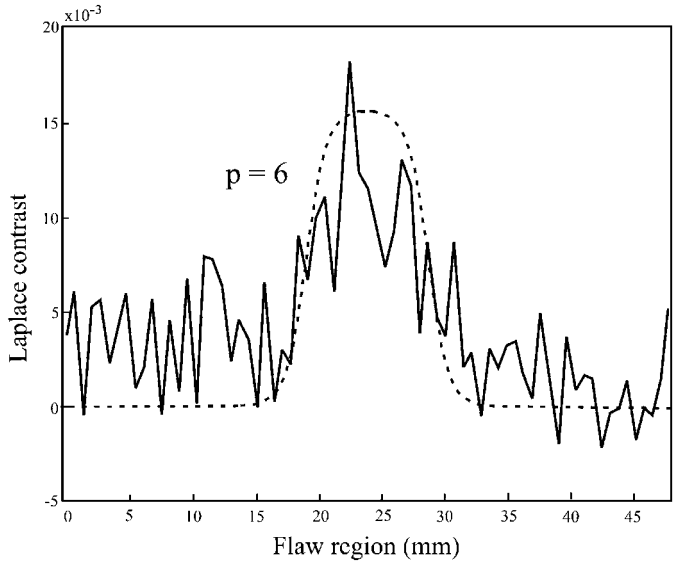

Figure 9. Experimental Laplace profile $\Delta\tau(x, z_s = 1, p = 6)$ across the defective region of the investigated sample (——) and theoretical Laplace profile (- - - -).

mid-depth of the investigated specimen should be around 125% when a p-value of 1 is used for the inversion (figure 3). Another possible reason for the too high estimated thermal resistance, $\varepsilon = 0.185$ instead of $\varepsilon = 0.073$ is more likely that air layers of a few micrometres could be trapped between the Teflon films or between the films and the composite matrix.

From figures 4 and 5, we can also note the existence of thermal gradients near the edges of the sample due to heat losses. Since our model does not take into account the lateral heat losses, the integration domain used during the averaging of the thermal contrast equation (18) is reduced to overcome the edge effects. The integration area $L \times \ell$ is taken equal to 45 mm $\times$ 45 mm instead of the whole area of the sample, which is 60 mm $\times$ 60 mm. For clarity reasons, let us remind the reader here that equations (19) and (20) are applicable even if heat transfer across the centre of the flaw is not one dimensional. A front face experiment and equation (28) applied for an optimum Laplace p variable of 1 lead to the determination of the depth of the flaw, $e_1 = 0.53$. This represents a deviation of only 6% from the true value $e_1 = 0.5$. This discrepancy is in good agreement with the statistical prediction described in subsection 2.3.2 and figure 4; the real deviation is of the same order as the predicted standard deviation of the estimation error, around 10%, during depth inversion using a p-value of 1.

Application of equation (19) with the previously calculated values of thermal resistance, $\varepsilon = 0.185$, and depth, $e_1 = 0.53$, allows the determination of the flaw area, $a \times b$. For this goal, an experimental Laplace contrast distribution has been calculated with a Laplace variable $p = 6$. A contrast profile that crosses the flaw centre is reported in figure 9; it could be observed that it is affected by an important measurement noise. The space averaging of the latter Laplace contrast yields an average value: $\Delta\bar{\tau} = -18 \times 10^{-4}$. If the subsurface flaw is square ($a = b$), its side a is derived from equation (19): $a = 8.9$ mm; the deviation from the nominal value is -11%. Application of equation (20) leads to $a = 10.9$ mm, which represents a deviation of 9% from the real value. These discrepancies are in good agreement with the prediction reported in subsection 2.3.3 and figure 5 where the predicted standard deviation for $p = 6$ is around 7%.

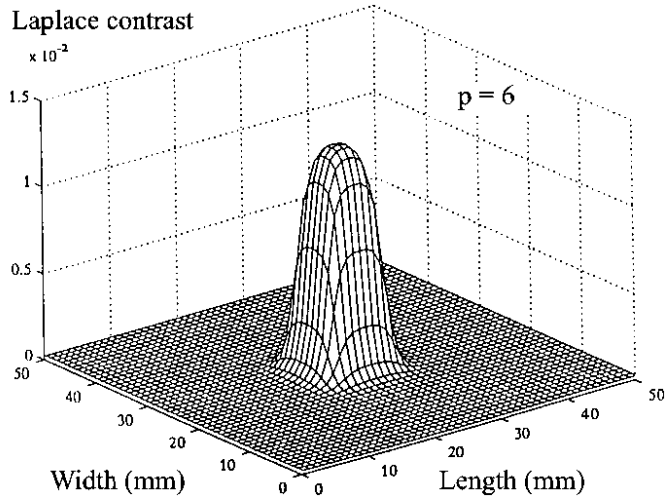

Figure 10. Theoretical Laplace distribution $\Delta\tau(x, y, z_s = 1, p = 6)$ calculated for a depth $e_1 = 0.5$, a lateral extent $a \times b = 10$ mm $\times$ 10 mm, and a thermal resistance $\varepsilon = 0.185$.

A simulated Laplace contrast field calculated with $p = 6$, $e_1 = 0.5$, $a = b = 10$ mm and $\varepsilon = 0.185$ is obtained using equation (15) and the inverse Fourier transform in equation (6). It is plotted in figure 10. A theoretical Laplace profile above the centre of the defective region is derived from the latter figure and reported in figure 9 together with the experimental profile. Comparison of these two profiles shows that the area affected by the Laplace contrast should be about 20 mm $\times$ 20 mm, which is not the case for the experiment where noise spreads outside this zone. Even with this large amount of measurement noise, the approach of averaging the thermal contrast allows us to reduce the effect of noise, and to give convenient estimations for the flaw parameters.

4. Conclusion

Unsteady three-dimensional heat diffusion within an anisotropic material containing a limited extent discontinuity has been solved using a perturbation expansion and integral transforms. The perturbation method has been used for its first order only to achieve a simple and fast approximation. Parameter estimation procedures based on the solutions obtained via the perturbation method have been implemented. The theoretical results were then validated on an artificial sample submitted to a stimulated infrared thermography test. The flaw was composed by the superimposition of two thin Teflon films. The estimated flaw depth and flaw lateral extent were very close to the nominal values of the artificial flaw. However, the flaw thermal resistance was more than twice as high than the nominal value. This was explained by air layers trapped between the Teflon films or between the Teflon films and the matrix of the composite material.

Appendix A. Effect of measurement noise on the Laplace contrast $\Delta\tau$

In practice, the measurements y_i carried out at times t_i ($i = 1$ to n) of the original normalized contrast always include a random noise ε_i caused by the infrared camera itself. The noisy

measurements can therefore be written

$$y_i = \Delta T_i + \varepsilon_i. \tag{A.1}$$

The calculation of the experimental Laplace transform of the original thermal contrast is performed using

$$m_{\exp j} = \sum_{i=1}^{n} y_i \exp(-p_j t_i)\Delta t = \sum_{i=1}^{n} \Delta T_i \exp(-p_j t_i)\Delta t + \sum_{i=1}^{n} \varepsilon_i \exp(-p_j t_i)\Delta t. \tag{A.2}$$

The subscript j (=1 or 2) corresponds to the Laplace variable p_j. We moreover assume that the error stemming from the quadrature is almost zero

$$\sum_{i=1}^{n} \Delta T_i \exp(-p_j t_i)\Delta t \cong \int_0^{\infty} \Delta T \exp(-p_j t_i)\,\mathrm{d}t. \tag{A.3}$$

In this case, the error on the Laplace transform is given by

$$e_{mj} = \sum_{i=1}^{n} \varepsilon_i \exp(-p_i t_i)\Delta t. \tag{A.4}$$

In order to take into account the two transforms ($j = 1$ and 2), the latter equation is written in a matrix form

$$\begin{pmatrix} e_{m1} \\ e_{m2} \end{pmatrix} = \begin{pmatrix} \sum_{i=1}^{n} \varepsilon_i \exp(-p_1 t_i)\Delta t \\ \sum_{i=1}^{n} \varepsilon_i \exp(-p_2 t_i)\Delta t \end{pmatrix}. \tag{A.5}$$

If we write $g_{ji} = \exp(-p_j t_i)\Delta t$, the latter matrix relationship becomes

$$\begin{pmatrix} e_{m1} \\ e_{m2} \end{pmatrix} = \begin{pmatrix} g_{11} & g_{12} & \cdots & g_{1n} \\ g_{21} & g_{22} & \cdots & g_{2n} \end{pmatrix} \begin{pmatrix} \varepsilon_1 \\ \varepsilon_2 \\ \cdots \\ \varepsilon_n \end{pmatrix} = (H)(\varepsilon). \tag{A.6}$$

The variance-covariance matrix of the Laplace contrast $m_{\exp}$ is then given by

$$\operatorname{cov}(m_{\exp}) = \operatorname{cov}(e_m) = H \operatorname{cov}(\varepsilon) H^t. \tag{A.7}$$

If we assume a non-correlated noise with a constant standard deviation σ, we can write

$$\operatorname{cov}(\varepsilon) = \sigma^2 I \quad (I \text{ is the identity matrix}) \tag{A.8}$$

and finally

$$\operatorname{cov}(e_m) = \sigma^2 H H^t. \tag{A.9}$$

This matrix multiplication leads to

$$\operatorname{cov}(e_m) = \sigma^2 (\Delta t)^2 \begin{pmatrix} \sum_{i=1}^{n} \exp(-2p_1 t_i) & \sum_{i=1}^{n} \exp(-(p_1 + p_2) t_i) \\ \sum_{i=1}^{n} \exp(-(p_1 + p_2) t_i) & \sum_{i=1}^{n} \exp(-2p_2 t_i) \end{pmatrix}. \tag{A.10}$$

Since we have neglected the quadrature error, the final result is obtained by

$$\operatorname{cov}(e_m) = \sigma^2 \Delta t \begin{pmatrix} \frac{1}{2p_1} & \frac{1}{p_1+p_2} \\ \frac{1}{p_1+p_2} & \frac{1}{2p_2} \end{pmatrix}. \tag{A.11}$$

Appendix B. Effect of measurement noise on the average Laplace contrast $\Delta\bar{\tau}$

The space averaging equation of the theoretical Laplace contrast is defined by

$$\Delta\bar{\tau} = \frac{1}{L\ell}\int_0^L \int_0^\ell \Delta\tau(x, y, z_s, p)\,\mathrm{d}x\,\mathrm{d}y. \tag{B.1}$$

The experimental average Laplace contrast is calculated using

$$\bar{m}(p) = \frac{1}{L\ell}\sum_{i=1}^{N}\sum_{j=1}^{M} m_{ij}(p)\Delta x\Delta y \tag{B.2}$$

where M is the number of pixels per line and N is the number of pixels by column in the infrared image, $\Delta x = \frac{L}{M}$ and $\Delta y = \frac{\ell}{N}$ are the lateral dimensions of each pixel.

If the original contrasts ΔT_{ij} are independent, then their Laplace transforms $m_{ij}(p)$ for a certain value of p are independent as well. In this case, the variance of the averaged contrast is calculated by

$$\mathrm{cov}(\bar{m}(p)) = \left(\frac{\Delta x\Delta y}{L\ell}\right)^2 \sum_{i=1}^{M}\sum_{j=1}^{N}\mathrm{cov}(m_{ij}(p)). \tag{B.3}$$

If the original contrast has the same variance, equation (B.3) yields the variance–covariance matrix of the average Laplace contrast

$$\mathrm{cov}(\bar{m}(p)) = \left(\frac{\Delta x\Delta y}{L\ell}\right)^2 NM\,\mathrm{cov}(m(p)) = \frac{\sigma^2\Delta t}{NM}\begin{pmatrix} \frac{1}{2p_1} & \frac{1}{p_1+p_2} \\ \frac{1}{p_1+p_2} & \frac{1}{2p_2} \end{pmatrix}. \tag{B.4}$$

Appendix C. Estimation error during flaw thermal resistance inversion

Thermal resistance ε is calculated with the following relationship:

$$\varepsilon = \frac{n_1^2\sinh(\sqrt{p_1})\tanh(\sqrt{p_1})}{n_2\cosh(\sqrt{p_1}) - n_1} \tag{C.1}$$

where

$$n_i = \Delta\tau(x_c, y_c, 1, p_i), \qquad i = 1, 2 \qquad \text{and} \qquad p_2 = 4p_1.$$

If the thermal contrast is noisy, the estimated thermal resistance is then obtained by the following expression:

$$\hat{\varepsilon} = \frac{\left(n_1 + e_{n_1}\right)^2\sinh(\sqrt{p_1})\tanh(\sqrt{p_1})}{\left(n_2 + e_{n_2}\right)\cosh(\sqrt{p_1}) - \left(n_1 + e_{n_1}\right)}. \tag{C.2}$$

If only the first-order terms are kept, the error on the estimated thermal resistance can be written under the following form:

$$e_\varepsilon = -\varepsilon\left(U e_{n_1} - V e_{n_2}\right) \tag{C.3}$$

with U and V given by

$$U = \frac{-n_1 + 2n_2\cosh(\sqrt{p_1})}{n_1[1 + n_1\sqrt{p_1}\sinh(\sqrt{p_1})][-n_1 + n_2\cosh(\sqrt{p_1})]} \tag{C.4}$$

$$V = \frac{[1 + n_1\sqrt{p_1}\sinh(\sqrt{p_1})]\cosh(\sqrt{p_1})}{[1 + n_2\sqrt{p_1}\sinh(\sqrt{p_2})][-n_1 + n_2\cosh(\sqrt{p_1})]}. \tag{C.5}$$

On the rear face, the thermal contrast in the linear case is given by

$$n_j = -\varepsilon \frac{\sinh(\sqrt{p_j}e_1)\sinh[\sqrt{p_j}(1-e_1)]}{\sinh^2(\sqrt{p_j})}, \qquad j = 1 \text{ or } 2. \tag{C.6}$$

After writing equation (C.3) in a matrix form and using equations (A.11) and (C.6), we can obtain the variance–covariance matrix of the thermal resistance

$$\sigma_\varepsilon^2 = \varepsilon^2\sigma^2\Delta t\,(U\,V)\begin{pmatrix} \frac{1}{2p_1} & \frac{1}{p_1+p_2} \\ \frac{1}{p_1+p_2} & \frac{1}{2p_2} \end{pmatrix}\begin{pmatrix} U \\ V \end{pmatrix}. \tag{C.7}$$

Appendix D. Estimation error during flaw depth inversion

The depth of the flaw is given by the following equation

$$e_1 = 1 - \frac{1}{\sqrt{p_1}}\ln\left[\left(\frac{\bar{m}_2}{\bar{m}_1}\right)^{1/2}\cosh(\sqrt{p_1}) + \left(\frac{\bar{m}_2}{\bar{m}_1}\cosh^2(\sqrt{p_1}) - 1\right)^{1/2}\right]. \tag{D.1}$$

If we take into account the noise added to the average thermal contrast, the previous equation yields

$$\hat{e}_1 = 1 - \frac{1}{\sqrt{p_1}}\ln\left[\left(\frac{\bar{m}_2 + e_{\bar{m}_2}}{\bar{m}_1 + e_{\bar{m}_1}}\right)^{1/2}\cosh(\sqrt{p_1}) + \left(\frac{\bar{m}_2 + e_{\bar{m}_2}}{\bar{m}_1 + e_{\bar{m}_1}}\cosh^2(\sqrt{p_1}) - 1\right)^{1/2}\right]. \tag{D.2}$$

If we keep only the first-order terms, the error on the flaw depth is obtained by

$$e_{e_1} = W\left(\frac{e_{\bar{m}_1}}{\bar{m}_1} - \frac{e_{\bar{m}_2}}{\bar{m}_2}\right) \tag{D.3}$$

where

$$W = \frac{\sqrt{\frac{\bar{m}_2}{\bar{m}_1}}\cosh\sqrt{p_1}\left(1 + \sqrt{\frac{\bar{m}_2}{\bar{m}_1}}\cosh\sqrt{p_1}\left(\frac{\bar{m}_2}{\bar{m}_1}\cosh^2\sqrt{p_1} - 1\right)^{-1/2}\right)}{2\sqrt{p_1}\left(\sqrt{\frac{\bar{m}_2}{\bar{m}_1}}\cosh\sqrt{p_1} + \sqrt{\frac{\bar{m}_2}{\bar{m}_1}\cosh^2\sqrt{p_1} - 1}\right)}.$$

In a matrix formulation, equation (D.3) becomes

$$e_{e_1} = \left(\frac{W}{\bar{m}_1} - \frac{W}{\bar{m}_2}\right)\begin{pmatrix} e_{\bar{m}_1} \\ e_{\bar{m}_2} \end{pmatrix}. \tag{D.4}$$

Using the relationships on covariances and equation (D.4), we can obtain the expression of the variance–covariance matrix of the flaw depth

$$\sigma_{e_1}^2 = \frac{\sigma^2\Delta t}{NM}W^2\left(\frac{1}{\bar{m}_1} - \frac{1}{\bar{m}_2}\right)\begin{pmatrix} \frac{1}{2p_1} & \frac{1}{p_1+p_2} \\ \frac{1}{p_1+p_2} & \frac{1}{2p_2} \end{pmatrix}\begin{pmatrix} \frac{1}{\bar{m}_1} \\ -\frac{1}{\bar{m}_2} \end{pmatrix}. \tag{D.5}$$

If we consider the linear case, the average Laplace contrast on the front face is defined by

$$\bar{m}_j = \frac{\varepsilon ab}{L\ell}\frac{\sinh^2[\sqrt{p_j}(1-e_1)]}{\sinh^2(\sqrt{p_j})}, \qquad \text{with} \quad j = 1 \text{ or } 2. \tag{D.6}$$

Finally, the expression of the variance on the flaw depth is calculated by

$$\sigma_{e_1}^2 = \frac{\sigma^2 \Delta t}{4NM\varepsilon^2}\left(\frac{L\ell}{ab}\right)^2 \frac{1}{p_1} \times \left\{\cosh(\sqrt{p_1}(1-e_1))\left(1+\frac{\cosh(\sqrt{p_1}(1-e_1))}{|\exp(\sqrt{p_1}(1-e_1))-\cosh(\sqrt{p_1}(1-e_1))|}\right) \times \exp(-\sqrt{p_1}(1-e_1))\right\}^2 \left(\frac{\sinh^4(\sqrt{p_1})}{2p_1\sinh^4(\sqrt{p_1}(1-e_1))}+\frac{\sinh^4(\sqrt{p_2})}{2p_2\sinh^4(\sqrt{p_2}(1-e_1))} - \frac{2}{p_1+p_2}\frac{\sinh^2(\sqrt{p_1})\sinh^2(\sqrt{p_2})}{\sinh^2(\sqrt{p_1}(1-e_1))\sinh^2(\sqrt{p_2}(1-e_1))}\right). \tag{D.7}$$

Appendix E. Estimation error during flaw area inversion

The area $S = ab$ of the flaw is calculated using the following equation:

$$S = \frac{L\ell}{\varepsilon}\frac{\sinh^2(\sqrt{p})}{\sinh(\sqrt{p}e_1)\sinh[\sqrt{p}(1-e_1)]}\bar{m}(p). \tag{E.1}$$

Its variance is therefore given by

$$\mathrm{var}(S) = \left[\frac{L\ell}{\varepsilon}\frac{\sinh^2(\sqrt{p})}{\sinh(\sqrt{p}e_1)\sinh[\sqrt{p}(1-e_1)]}\right]^2 \mathrm{var}(\bar{m}(p)). \tag{E.2}$$

Combination of equations (B.4) and (E.2) leads to

$$\mathrm{var}(S) = \frac{\sinh^4(\sqrt{p})}{\sinh^2(\sqrt{p}e_1)\sinh^2[\sqrt{p}(1-e_1)]}\left(\frac{L\ell}{\varepsilon}\right)^2 \frac{\sigma^2}{NM}\frac{\Delta t}{2p}. \tag{E.3}$$

If the flaw has a square shape, $a = b$ and $S = a^2$, the variance of the lateral extent a can be obtained by

$$\mathrm{var}(a) = \frac{\mathrm{var}(S)}{4}. \tag{E.4}$$

References

[1] Vavilov V 1992 Thermal nondestructive testing: short history and state of the art *Quantitative Infrared Thermography Conf. (Châtenay-Malabry, France)* pp 179–89

[2] Maldague X 2000 Applications of infrared thermography in nondestructive evaluation *Trends in Optical Nondestructive Testing* ed P K Rastogi and D Inaudi (Amsterdam: Elsevier)

[3] Maldague X 1999 Pipe inspection by infrared thermography *Mater. Eval.* **57** 899–902

[4] Galmiche F and Maldague X 1999 Active infrared thermography for land mine detection *Proc. SPIE* **3827** 146–54

[5] Bendada A 2004 Nondestructive thermography inspection of scuff-resistant coating adhesion flaws in automobile engine block cylinders *J. Adhes. Sci. Technol.* **18** 943–50

[6] Bendada A, Maillet D, Batsale J C and Degiovanni A 1998 Reconstitution of a non uniform interface thermal resistance by inverse heat conduction—application to infrared thermography testing *Inverse Problem Eng.* **6** 79–123

[7] Degiovanni A, Bendada A, Batsale J C and Maillet D 1994 Analytical simulation of a three-dimensional temperature field produced by planar defects of any shape: application to nondestructive testing *Quantitative Infrared Thermography Conf. (Sorrento)* pp 251–9

[8] Avdelidis N P and Almond D P 2004 Through skin sensing assessment of aircraft structures using pulsed thermography *NDT&E Int.* **37** 353–9

[9] Ball R J and Almond D P 1998 The detection and measurement of impact damage in thick carbon fibre reinforced laminates by transient thermograhy *NDT&E Int*. **31** 165–73
[10] Almond P and Peng W 2001 Thermal imaging of composites *J. Microsc*. **201** 163–70
[11] Wu D T and Busse G 1998 Lock-in thermography for nondestructive evaluation of materials *Int. J. Therm. Sci*. **37** 693–703
[12] Diener L, Steegmuller R, Wu D and Busse G 1996 Characterization of microwave near-zone field by using lock-in thermography *Prog. Nat. Sci*. **6** (Suppl. S) S95–8
[13] Wu D and Busse G 1996 Remote inspection of wood with lock-in thermography *TAPPI J*. **79** 119–23
[14] Schroeder J A, Ahmed T, Chaudhry B and Shepard S 2002 Non-destructive testing of structural composites and adhesively bonded composite joints: pulsed thermography *Composites* A **33** 1511–7
[15] Beck J V, Blackwell B and St Clair C R Jr 1985 *Inverse Heat Conduction* (New York: Wiley)
[16] Tikhonov A N and Arsenin V Y 1977 *Solutions of Ill-Posed Problems* (Washington, DC: Winston)
[17] Alifanov O M 1994 *Inverse Heat Transfer Problems* (Berlin: Springer)
[18] Maillet D, André S, Batsale J C, Degiovanni A and Moyne C 2000 *Thermal Quadrupoles: Solving the Heat Equation Through Integral Transforms* (Chichester: Wiley)
[19] Bush A W 1992 *Perturbation Methods for Engineers and Scientists* (Boca Raton, FL: CRC Press)
[20] Aziz A and Na T 1984 *Perturbations Methods in Heat Transfer* (Berlin: Springer)
[21] Hagen K D 1987 A solution to unsteady conduction in periodically layered composite media using a perturbation method *J. Heat Transfer* **109** 1021–3
[22] Nayfeh A H 1973 *Perturbation Methods* (New York: Wiley)
[23] Maillet D, Philippi I, Bendada A and Degiovanni A 1998 Integral transforms and parameter estimation in diffusive transfer *Inverse Problems in Engineering: Theory and Practice (Le Croisic, France)* pp 463–71
[24] Leturcq P, Dorkel J M, Ratolojanarhary F E and Tounsi S 1993 A two-port network formalism for 3D heat conduction analysis in multilayered media *Int. J. Heat Mass Transfer* **36** 2317–26
[25] Bendada A 1995 Tomographie infrarouge stimulée: estimation d'une résistance d'interface non uniforme *PhD Thesis* Institut National Polytechnique de Lorraine
[26] Stehfest H 1970 Remarks on algorithm 368, numerical inversion of Laplace transforms *Commun. ACM* p 624
[27] Maillet D, Houlbert A S, Didierjean S, Lamine A S and Degiovanni A 1993 Non-destructive thermal evaluation of delaminations in a laminate: I. Identification by measurement of thermal contrast *Composites Sci. Technol*. **47** 137–53
[28] Bendada A 2002 Approximate solutions to three-dimensional unsteady heat conduction through plane flaws within anisotropic media using a perturbation method *Modelling Simul. Mater. Sci. Eng*. **10** 673–84
[29] Bendada A, Maillet D and Degiovanni A 1992 Non destructive transient thermal evaluation of laminated composites: discrimination between delaminations thickness variations and multi-delaminations *Quantitative Infrared Thermography Conf. (Châtenay-Malabry, France)* pp 218–23
[30] Baker G A 1965 The theory and application of Padé approximant method *Advances in Theoretical Physics* (New York: Academic) pp 1–58
[31] Houlbert A S, Lamine A S and Degiovanni A 1991 Modélisation d'un défaut limité en vue du contrôle non destructif des matériaux anisotropes *Int. J. Heat Mass Transfer* **34** 1125–38
[32] Bendada A 2001 Quantitative Inversion and Discontinuity Characterization*Nondestructive Testing Handbook: Infrared and Thermal Testing* (Columbus, OH: American Society for Nondestructive Testing) pp 273–385